Insights into higher twist in nucleon from measurements of g_2 structure function

P. Solvignon
Argonne National Laboratory, Argonne, IL

E. Brash
Christopher Newport University, Newport News, VA and
Thomas Jefferson National Accelerator Facility, Newport News, VA

P. Carter and M. Veilleux
Christopher Newport University, Newport News, VA

A. Puckett

W. Boeglin, P. Markowitz, and J. Reinhold
Florida International University, Miami, FL

I. Albayrak, O. Ates, C. Chen, M. E. Christy, C. Keppel, M. Kohl, Y. Li,
A. Liyanage, P. Monaghan, X. Qiu, L. Tang, T. Walton, Z. Ye, and L. Zhu
Hampton University, Hampton, VA

M. K. Jones, P. Bosted, J.-P. Chen, S. Covrig, W. Deconink, A. Deur, C. Ellis, R.
Ent, D. Gaskell, J. Gomez, D. Higinbotham, T. Horn, D. Mack, G. Smith, and S. Wood
Thomas Jefferson National Accelerator Facility, Newport News, VA

J. Dunne, D. Dutta, A. Narayan, L. Ndukum, and Nuruzzaman
Mississippi State University, Jackson. MI

A. Ahmidouch, S. Danagoulian, B. Davis, J. German, and M. Jones
North Carolina A&M State University, Greensboro, NC

M. Khandaker
Norfolk State University, Norfolk, VA

A. Daniel, P.M. King, and J. Roche
Ohio University, Athens, OH

A.M. Davidenko, Y.M. Goncharenko, V.I. Kravtsov, Y.M. Melnik, V.V. Mochalov, L. Soloviev, and A. Vasiliev
Institute for High Energy Physics, Protvino, Moscow Region, Russia

C. Butuceanu and G. Huber
University of Regina, Regina, SK

V. Kubarovsky
Rensselaer Polytechnic Institute, Troy, NY

L. El Fassi and R. Gilman
Rutgers University, New Brunswick, NJ

S. Choi, H-K. Kang, H. Kang, and Y. Kim
Seoul National University, Seoul, Korea

W. Armstrong, D. Flay, Z.-E. Meziani, M. Posik, B. Sawatzky, and H. Yao
Temple University, Philadelphia, PA

O. Hashimoto, D. Kawama, T. Maruta, S. Nue Nakamura, and G. Toshiyuki
Tohoku U., Tohoku, Japan

K. Slifer
University of New Hampshire

H. Baghdasaryan, M. Bychkov, D. Crabb, D. Day, E. Frlez, O. Geagla, N. Kalantarians, K. Kovacs, N. Liyanage, V. Mamyan, J. Maxwell, J. Mulholland, D. Pocanic, S. Riordan, O. Rondon, and M. Shabestari
University of Virginia, Charlottesville, VA

L. Pentchev
College of William and Mary, Williamsburg, VA

F. Wesselmann
Xavier Unniversity, New Orleans, LA

A. Asaturyan, A. Mkrtchyan, H. Mkrtchyan, and V. Tadevosyan
Yerevan Physics Institute, Yerevan, Armenia

W. Luo
Lanzhou University, Lanzhou 730000, Gansu, People's Republic of China
(Dated: March 19, 2015)

The Spin Asymmetries of the Nucleon Experiment (SANE) measured the parallel, $A_{\parallel}$, and near-perpendicular, A_{80}, double spin asymmetries in inclusive polarized electron scattering on a polarized proton. The scattered electrons were detected using the Big Electron Telescope Array, BETA, which was centered at 40° and covered a large solid angle. BETA consisted of a scintillator hodoscope, gas Cherenkov, lucite hodoscope and a large array of lead glass detectors. The data was taken at the Thomas Jefferson Lab National Accelerator Facility's Hall C at beam energies of 4.7 and 5.9 GeV and covered $2.5\ GeV^2 < Q^2 < 6.5\ GeV^2$. From the $A_{\parallel}$ and A_{80} measurements, the proton's spin asymmetries, A_1 and A_2, and the spin structure functions of the proton, g_1 and g_2, can be extracted. The measurements are in a range of Bjorken x, $0.3 < x < 0.8$, where extraction of the twist three matrix element d_2^p (an integral of g_1 and g_2 weighted by x^2) is most sensitive.

I. INTRODUCTION

After more than 30 years of experimental and theoretical work, the study of the nucleon spin structure has entered a mature stage, extending beyond the exploration of the properties of the polarized structure functions in the scaling regime into the region of the Bjorken scaling variable x near its unity upper limit. Moreover, the experimental techniques have expanded from the original simple approach of measuring double spin asymmetries in inclusive deep inelastic scattering - DIS [1–6] for parallel beam and target spins, or even for parallel and orthogonal configurations [7–11], to semi-inclusive measurements with detection of a π or K meson in coincidence with the scattered electron [12, 13] and the investigation of the gluon polarization [14, 15]. From the inclusive measurements in DIS it has been established that the quarks carry only about 25% of the nucleon spin, and from the inclusive and semi-inclusive measurements, the quark polarization by flavor has been determined [12, 16, 17].

The modern description of nucleon structure is done in terms of transverse momentum dependent quark distributions functions [18] defined in terms of quark-quark (qq) and quark-gluon-quark(qgq) correlations in the nucleon. Two of the leading twist distributions from qq correlations translate, after integration over the transverse momentum $\vec{k}_{\perp}$, into the more familiar structure functions (SF) measured in DIS. The longitudinal momentum distribution $q(x, k_T^2)$ (also known as f_1) leads to the unpolarized SF $F_1(x, Q^2)$, which is a function of the Bjorken scaling variable x and the four-momentum transfer squared $Q^2 = -q_\mu^2$. The quark helicity distribution $\Delta q(x)$ (or g_{1L}) is related to the spin SF $g_1(x, Q^2)$. These distributions have quark flavor indices associated with them and the nucleon structure functions are linear combinations of all active flavors, weighted by their charges squared.

At subleading twist-3, there are two k_T-integrated distributions related to qq correlations, namely $g_T(x)$ and $h_L(x)$. In addition, at the same twist-3 $\mathcal{O}(1/Q)$, three-particle qgq correlations lead to the corresponding distributions $\tilde{g}_T(x)$ and $\tilde{h}_L(x)$.

The transverse distribution $g_T(x)$ is of particular interest, because it can be measured in inclusive double polarized DIS with target polarization transverse to the beam helicity. In terms of the k_T dependent distribution $g_{1T}(x, k_T^2)$, $g_T(x)$ is given by [19, 20]

$$g_T(x) = \int d^2k_T \frac{k_T^2}{2M^2} \frac{g_{1T}(x, k_T^2)}{x} + \frac{m}{M}\frac{h_1(x)}{x} + \tilde{g}_T(x), \tag{1}$$

where the $h_1(x)$ term represents the contribution of the transversity distribution (net transverse quark spin in a transversely polarized nucleon), that is suppressed in DIS by the ratio of the quark to nucleon masses, m/M.

This expression highlights the importance of transverse quark momentum even in inclusive measurements: g_T would be negligibly different from the qgq-correlations dependent $\tilde{g}_T$ without transverse momentum In fact, carrying out the integration of g_{1T} expressed in terms of Lorentz invariant amplitudes [20] one can obtain

$$g_T(x) = \int_x^1 dy \frac{g_1(y)}{y} + \frac{m}{M}\Big[\frac{h_1(x)}{x} - \int_x^1 dy \frac{h_1(y)}{y}\Big] + \tilde{g}_T(x) - \int_x^1 dy \frac{\tilde{g}_T(y)}{y}. \quad (2)$$

where the first term depends only on the twist-2 quark helicity distribution g_1, which is definitely not zero.

The mixed twist (2 and 3) nature of gT arises from the contribution of the $\tilde{g}_T$ terms. As it would be expected, the same terms contribute to the $g_2(x, Q^2)$ SF, which dominates the difference of cross sections in DIS with polarized beams on a transversely polarized target

$$\Delta\sigma = \frac{4\alpha^2 E'^2}{ME(E-E')Q^2} \sin\theta\cos\phi\Big(g_1(x,Q^2) + \frac{2E}{E-E'}\, g_2(x,Q^2)\Big) \quad (3)$$

This unique feature of transverse polarized scattering allows direct access to sub-leading, twist-3 processes in a direct measurement [21].

In terms of the g_1 and g_2 SF's, g_T can be written simply as

$$g_T(x,Q^2) = g_1(x,Q^2) + g_2(x,Q^2) \quad (4)$$

The result for the twist-2 part of g_2 found by Wandzura and Wilczeck [22]

$$g_2^{WW}(x,Q^2) = -\, g_1(x,Q^2) + \int_x^1 g_1(y,Q^2)\frac{dy}{y} \quad (5)$$

corresponds to the first term of g_T in eq. (2).

The structure of the nucleon can also be described in terms of forward virtual Compton scattering. The virtual Compton scattering spin asymmetry (SA) $A_2(x,Q^2) = \sigma_{LT}/\sigma_T$, is formed from the longitudinal-transverse interference cross section σ_{LT} and the transverse cross section σ_T for the scattering of polarized electrons on polarized nucleons. In terms of A_2, g_T can be expressed as

$$g_T(x,Q^2) = \frac{E-E'}{\sqrt{Q^2}} F_1(x,Q^2) A_2(x,Q^2) \quad (6)$$

g_T can then be understood as being a measure of the polarization of quarks with spins perpendicular to the virtual photon helicity.

g_T can also be identified as the polarized partner of the unpolarized longitudinal $F_L(x,Q^2) = 2xF_1R$, which has a similar form in terms of F_1 and the ratio of the longitudinal to transverse virtual photon cross sections $R = \sigma_L/\sigma_T$. F_L is zero at leading twist but becomes nonzero through higher twist effects resulting from non-zero parton transverse momentum, which give rise to finite values of σ_L.

With the suppression of h_1 by the ratio m/M[23–25]. the third moment of the interaction dependent part $\tilde{g}T$ can be related by the operator product expansion (OPE) to the reduced twist-3 quark matrix element d_2

$$\overline{g}_2(x) = \tilde{g}_T(x) - \int_x^1 dy \frac{\tilde{g}_T(y)}{y}$$
$$\int_0^1 x^2 \overline{g}_2(x,Q^2)dx = \frac{1}{3} d_2(Q^2), \quad (7)$$

which can be calculated in lattice QCD [26]. However, it should be kept in mind that since h_1 is a leading twist quantity (comparable in magnitude to g_1), even if the ratio m/M were of the order of $\sim 1\%$, h_1 could represent a significant contribution to $\overline{g}_2$.

Only a handful of measurements of d_2 exist to date, from SLAC [7, 10, 11], and from RSS [27] at Jefferson Lab. The SLAC measurements have been combined into a single number for the proton $d_2(Q^2 = 5\ \mathrm{GeV}^2) = 0.0032 \pm 0.0017$. The lattice QCD result at the same Q^2 is $d_2 = 0.004 \pm 0.005$. The RSS proton result covers a wide range of x from 0.29 to 0.84, corresponding to the region of the resonances from $W = 1.91$ GeV to the pion production threshold. Using Nachtmann moments, which are required to correct for the target recoil at low Q^2, the RSS result including the elastic contribution is $d_2(Q^2 = 1.3\ \mathrm{GeV}^2) = 0.0104 \pm 0.0014$ (total error).

In addition to lattice QCD, QCD sum rules [28–30], bag [31] and chiral quark models [32, 33] can also be tested by comparing their predictions to the measured moments of g_2. Moreover, g_2 gives access to the polarizabilities of the color fields [34] (with additional knowledge of the twist-4 matrix element f_2). The magnetic and electric polarizabilities are $\chi_B = (4d_2 + f_2)/3$ and $\chi_E = (2d_2 - f_2)/2$, respectively. Knowledge of these properties of the color fields is an important step in understanding QCD. The twist-4 f_2 matrix element represents quark-quark interactions, and reflects the higher twist corrections to the individual proton and neutron moments of g_1 and in consequence, to the Bjorken sum rule [35]

$$\int_0^1 g_1(x,Q^2)dx = \frac{1}{2}a_0 + \frac{M^2}{9Q^2}\big(a_2 + 4d_2 + 4f_2\big) + O\Big(\frac{M^4}{Q^4}\Big). \quad (8)$$

These matrix elements are related to the higher moments of the SSF's, which have a strong dependence on the high x contributions.

From an experimental point of view, the measurement of A_2 is simpler than that of the absolute cross section difference for scattering of longitudinally polarized electrons on transversely polarized nucleons, which is required to access g_2 directly. Therefore, it is easier to measure the parallel $A_\parallel$ and perpendicular $A_\perp$ asymmetries which are related to the spin asymmetries A_1 and A_2 by

$$A_1 = \frac{1}{(E+E')D'}\left((E - E'\cos\theta)A_\parallel - \frac{E'\sin\theta}{\cos\phi}A_\perp\right)$$
$$A_2 = \frac{\sqrt{Q^2}}{2ED'}\left(A_\parallel + \frac{E - E'\cos\theta}{E'\sin\theta\cos\phi}A_\perp\right) \qquad (9)$$

where all quantities (θ and ϕ are the scattered lepton's polar and azimuthal angles, respectively) are measured in the same experiment, with the exception of the small contribution from the unpolarized structure function $R(Q^2, W) = \sigma_L/\sigma_T$ to the virtual photon depolarization $D' = (1-\varepsilon)/(1+\varepsilon R)$. Here $\varepsilon = 1/(1 + 2(1 + \nu^2/Q^2)\tan^2(\theta/2))$ is the well known longitudinal polarization of the virtual photon. These expressions are suitably modified for the case when the beam and target spins aren't exactly perpendicular.

II. EXPERIMENT

A. Beam

B. DAQ

C. Polarized Target

SANE utilized frozen ammonia ($^{14}NH_3$) as a proton target, polarized via dynamic nuclear polarization (DNP) in a 5 T magnetic field at around 1 K. DNP is a mature technique for target polarization in the study of nuclear structure[1], and this target has had extensive use at SLAC [2–4] and Jefferson Lab [5]. Nuclear target polarizations of greater than 90% are achieved by leveraging electron–proton spin coupling in a high magnetic field, using microwaves to excite the spin flip transitions. The open-geometry of the superconducting, split-pair magnet allowed polarization both longitudinally and transverse to the electron beam incidence.

1. Dynamic Nuclear Polarization

Figure 1 shows a simplified diagram of the DNP mechanism. In a target material with a suitable number of unpaired electron spins, hyper-fine splitting from the spin-spin interaction of the proton and electron in the magnetic field gives four discrete energy levels. The spins of the electron and proton can be simultaneously flipped by applying microwaves of frequency lower or higher than the electron paramagnetic resonance by the proton magnetic resonance, which will result in the protons becoming aligned or anti-aligned, respectively, with the magnetic field. The electron will tend to relax into the lowest energy state, allowing it to be used to polarize another proton, making possible a continual driving of protons into positive polarization.

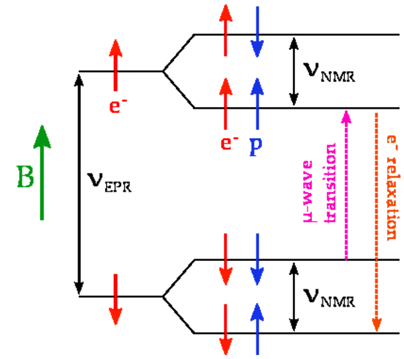

FIG. 1. Simplified diagram of the dynamic nuclear polarization mechanism.

At low temperature, the spin relaxation time of the protons is many times greater than that of the electrons; while the protons maintain their spin orientation, the electrons relax and can spin couple with other protons. This creates a rate of polarization higher than the rate of depolarization due to proton relaxation and allows polarization to be constantly built and maintained by microwaves.

Neighboring nuclear spins are coupled by dipole–dipole interactions which allow spin flips which conserve energy. These flips are thus frequently occurring, and allow for the transport of nuclear polarization away from the unpaired electrons. This process, called spin diffusion, tends to equalize the polarization throughout the material[6].

2. NMR Polarization Measurements

An accurate measure of the degree of the material's nuclear polarization is obtained through nuclear magnetic resonance measurements. An RF field at the proton's Larmor frequency will induce the spin system to either absorb or emit energy. The magnetic susceptibility of the system describes this absorption/emission response, and the integral over frequency of the absorptive portionof the susceptibility is proportional to the absolute polarization of the material.

By embedding an NMR coil in the target material, inductive coupling between the spins and the coil results in an impedance which is a function of the magnetic susceptibility[7]. Integrating the voltage due to this impedance with a Q-meter[8] as the RF is swept through frequency gives proportional measure of the absorptive part of the magnetic susceptibility, after the baseline behavior of the circuit is removed.

The polarization obtained by the NMR signal integration must be calibrated using the calculable polarization of the material at thermal equilibrium P_{TE}. When the material is allowed to relax to thermal equilibrium at known temperature T and magnetic field B, the proton polarization is due only to the Zeeman interaction between the field and the proton magnetic moment μ, and is thus known via Boltzmann statistics:

$$P_{\rm TE} = \tanh\left(\frac{\mu B}{kT}\right).$$

By integrating the Q-meter response curve at thermal equilibrium, the area obtained $A_{\rm TE}$ allows the calculation of the polarization during dynamic polarization with enhanced area $A_{\rm Enh}$: $P_{\rm Enh} = P_{\rm TE}A_{\rm Enh}/A_{\rm TE}$.

3. Material Preparation and Performance

Irradiated ammonia ($^{14}NH_3$) is an attractive target material due to its high polarizability and radiation hardiness, as well as its favorable ratio of free, polarizable protons to total nucleons—dilution factor. Ammonia freezes at 195.5 K, and can be crushed through a metal mesh to produce beads of convenient size, allowing cooling when the material is under a liquid helium bath[**?**].

Before DNP is feasible, the ammonia must first be doped with paramagnetic centers, which provide the crucial free electrons used for spin coupling to the protons; for SANE, the target material was irradiation doped at a small electron accelerator. Free radicals were created by 19 MeV electrons at a beam current of between 10 to 15 μA which struck the frozen ammonia in a 87 K LAr_2 bath, until an approximate dose of 10^{17} e^-/cm^2 was achieved.

After irradiation, proton polarizations in ammonia can routinely surpass 90% under dynamic nuclear polarization, however when used experimental conditions, the electron beam will cause depolarization. Beam heating will create a reduction in polarizing efficiency, and reduce the polarization by as much 5% in a matter of seconds[9]. Over hours of beam on target, excess free radicals are built up in the material which provide extra decay paths for the proton spin, and these radicals become the primary source of depolarization. This radiation damage of the material with electron dose from the beam appears as two or three exponential decays in the polarization vs. dose accumulated.

To recover the polarization lost to radiation damage the material can be "annealed" by heating it to between 70 to 100 K, allowing the recombination of certain free radicals. This process will often allow the polarization to achieve its previous maximal values, although the build-up of different radicals with subsequent anneals will result in the increased decay rate of the polarization, when the material must be replaced[10].

In the more than 300 hours of beam on target taken during SANE, 23 thermal equilibrium calibrations were taken, 26 anneals performed, and 7 material replacements were required for the 11 different samples of frozen ammonia target material used.

D. BETA

1. BigCal

2. Gas Čerenkov

The gas Čerenkov used 8 mirrors to focus...

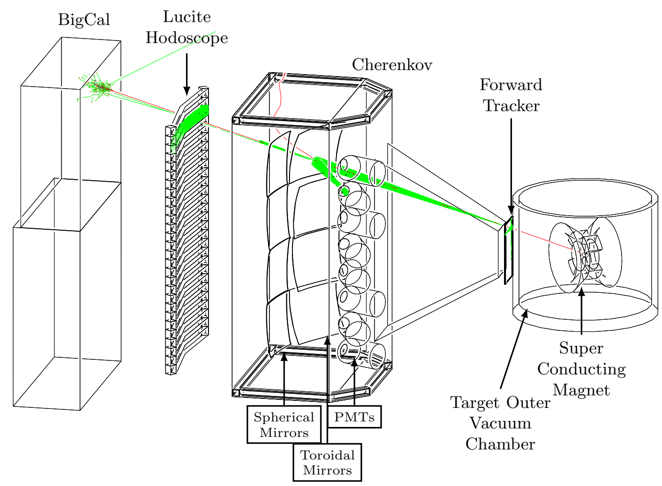

FIG. 2. Caption here

3. Lucite

4. Tracker

III. DATA ANALYSIS

A. Bigcal calibration

IV. BIGCAL CLUSTERS

The analyzer output for BigCal is a 56 by 32 matrix with energies for each block. For energy reconstruction, we first define a cluster as a 5 by 5 matrix of the blocks surrounding the most energetic one.

To find clusters, the block with maximum energy is identified (parent block). Next, the energies of blocks surrounding the parent block are recorded, as illustrated schematically in Figure 3, forming a 5 by 5 matrix which is defined as a cluster. As the detector consists of two parts (Protvino and RCS) with different block sizes, there can be mixed clusters where the matrix is not geometrically symmetric, with an example shown on Figure 3. When a cluster is identified, the energies of the 25 blocks are set to zero in the original 56 by 32 matrix, and the procedure is repeated to find additional clusters.

The criteria for cluster identification are:

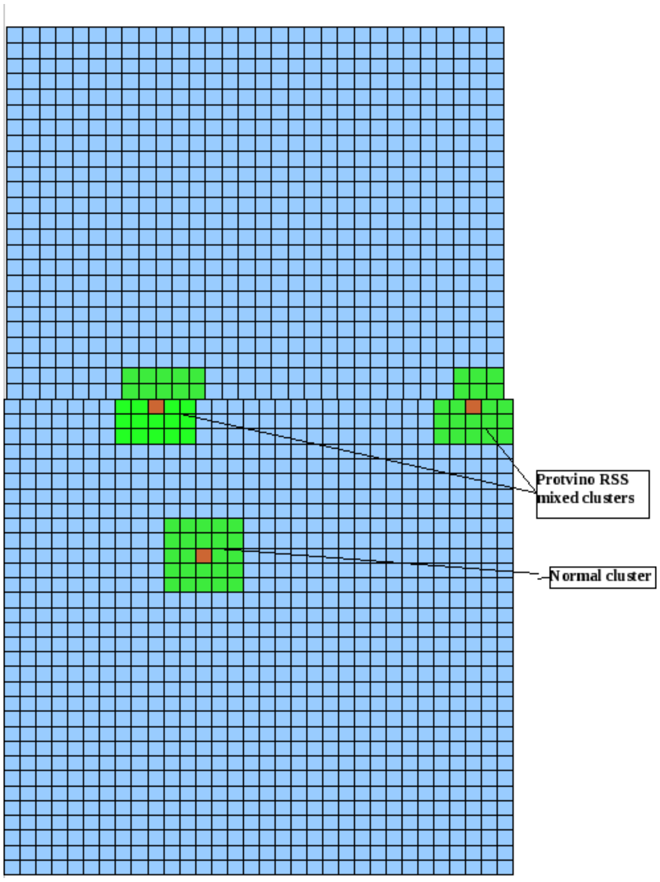

FIG. 3. BigCal cluster identification.

- Minimum energy of the block must be greater than 10 MeV
- Minimum energy of parent block equal to 50 MeV
- Minimum cluster energy equal to 150 MeV
- Minimum number of blocks in the cluster with energies greater than 10 MeV must be greater than 2

It was found during the analysis that the traditional methods of coordinate reconstruction, e.g. Eq. 10, where X_i and E_i correspond to the centroid coordinate and energy of the block i, which is used to calculate the energy weighted cluster centroid in the X coordinate, were failing, especially when the number of cells involved was small.

$$\langle X \rangle = \sum_i \frac{X_i/E_i^2}{1/E_i^2} \tag{10}$$

The PMTs gain calibration was being affected by poor coordinate reconstruction. During the gain calibration for BigCal we noticed that π^0 mass, reconstructed from two photon events drifted with photon energy. This effect could come either from an unexpected drift in gain parameters, from wrong coordinate reconstruction done with to the conventional clustering algorithms, or from the complicated dependence on gain parameters. To avoid the problem with incorrect coordinate reconstruction and to take into account the cuts on minimum energy of the BigCal block we decided to use a neural network (NN) method.

As input to the NN we used the energy of all 25 (5 by 5) blocks in a cluster, and the parent block's row iX and column iY (in the 32 by 56 blocks matrix). Using CERN's GEANT3 simulation tool [**??**], we generated six million electron events and six million photon events to train the network. The photons were generated to obtain the right calibration of the BigCal detector. Photon clusters are different from electron clusters due to the effect of the target's magnetic field on electrons, and the fact that photon showers start about one radiation length deeper in the lead glass than electron showers.

The neural network is based on a standard ROOT package [**??**] (TMultiLayerPerceptron). The NN has one hidden layer with 10 neurons and three outputs, dX, dY and dE, as shown in Figure 4 where dX and dY are coordinate corrections to the parent block's center and dE is an energy correction to the total energy of the cluster. The neuron training functions was chosen to be a

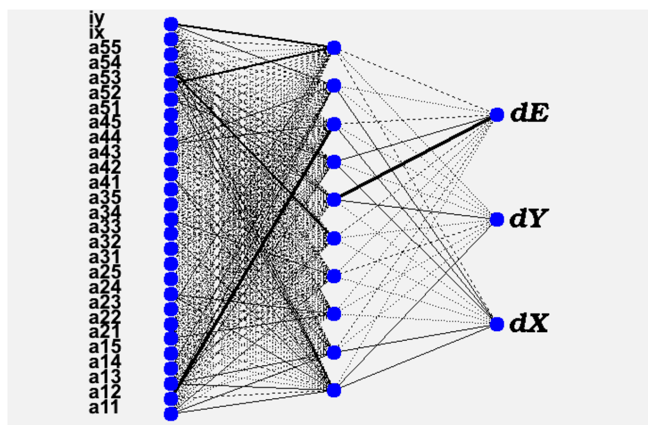

FIG. 4. Neural network structure.

Gaussian and the learning method to be KBFGS. Figure 5 shows the coordinate and energy resolutions before and after corrections. Coordinate reconstruction resolution using the NN is about 3 times better than that of conventional methods.

We also observed that to remove the dependence of the reconstructed pion mass on cluster energy we need to use $E_{clust} = \sum E_i \dot{g}_i + dE$ instead of $E_{clust} = \sum E_i \dot{g}_i$ where g_i is the gain parameter for the block and dE is the output of the NN .

The NN provided the corrected coordinates at BigCal. Due to the magnetic field, the angles for charged particles at the target are different from the angles obtained from a straight line connecting the target coordinate to BigCal's coordinate. To correct for the effect of the field, electron

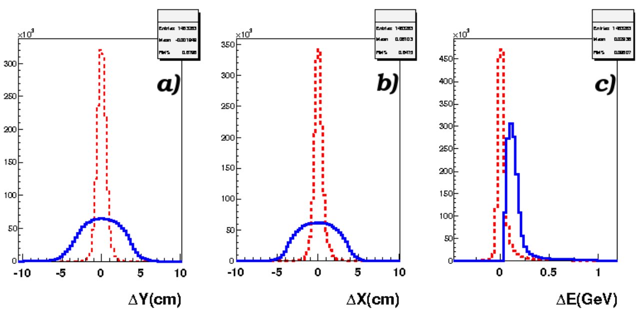

FIG. 5. Coordinate and energy resolutions before and after corrections.

events were generated using GEANT for different field orientations and the correction to the straight line angles was obtained using the following fit function

$$(\theta_t, \phi_t) = (\theta_s, \phi_s) \cdot 180/\pi \\ + (p_1 + p_2 \cdot \theta_s + p_3 \cdot \phi_s + p_4 \cdot \theta_s^2 + p_5 \cdot \phi_s^2 + p_6 \cdot \theta_s \cdot \phi_s) \\ (p_7 + p_8/E + p_9/E^2)(p_{10} + p_{11} \cdot X_r + p_{12} \cdot X_r^2) \quad (11)$$

where θ_s, ϕ_s are angles reconstructed using the straight line approximation, θ_t,ϕ_t are angles at the target, E is the energy of the cluster, and X_r and Y_r are raster coordinates. Figures 6 and 7 show polar angle reconstruction using the straight line approximation and the fit procedure, respectively. Figures 8 and 9 show the corresponding results for azimuthal angle reconstruction. The angular resolutions obtained using the NN fit are 0.5 degree for the polar angle and 1 degree for the azimuthal one.

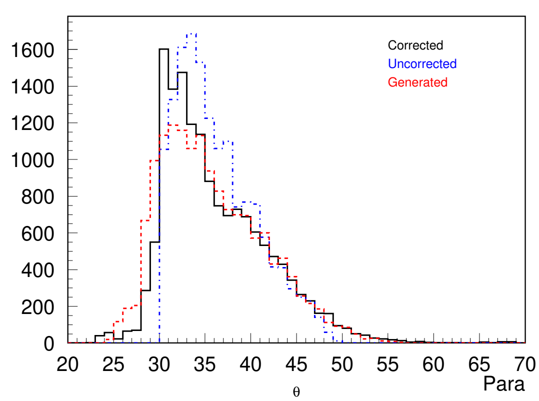

FIG. 6. Reconstruction of the polar angle using the fit for the parallel field configuration. The (red) dashed line is the generated spectrum, the (blue) dash-dotted line is the reconstructed spectrum using the straight line approximation, and the (black) solid line is the reconstructed spectrum using the fit.

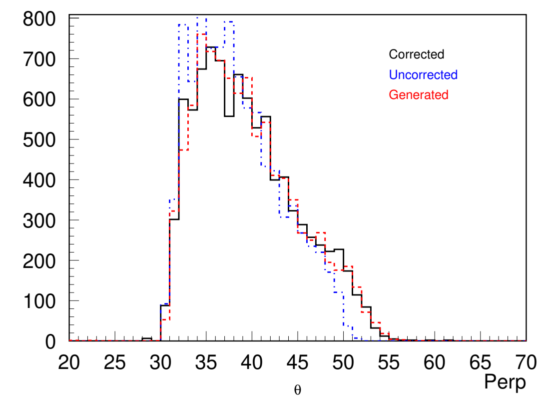

FIG. 7. Reconstruction of the polar angle using the fit for the perpendicular field configuration. The line styles are the same as in Fig.6

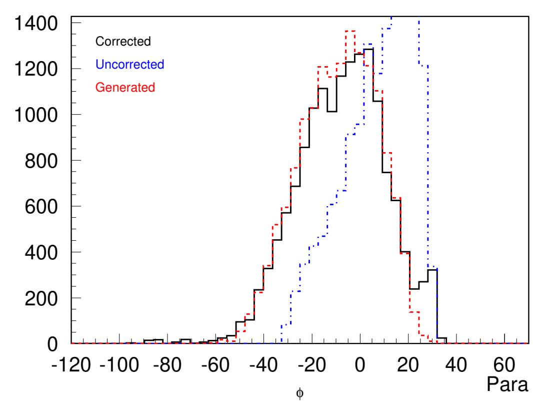

FIG. 8. Reconstruction of the azimuthal angle using the fit for the parallel field configuration. The line styles are the same as in Fig.6

To calibrate BigCal's PMT gains we used neutral pion events. The events were selected from the data by choosing events with two neutral clusters (no Cerenkov signal). In addition we applied cuts on minimum energy of the cluster, $E_{cluster} > 0.6$ GeV, and on the number of non-zero energy cells in a cluster, $N_{cell} > 4$, for improved position reconstruction. Using the NN the energies of the clusters were corrected for arbitrary gain parameters, and the invariant mass of the events was calculated. The invariant mass of the event was assigned to the most energetic block in the cluster. The assumption is that the most energetic block (as in average it carries more than 50 percent of the cluster energy) is responsible for any deviation from the known pion mass. The position

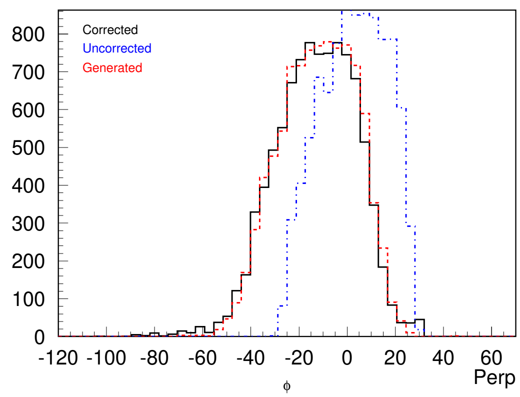

FIG. 9. Reconstruction of the azimuthal angle using the fit for the perpendicular field configuration. The line styles are the same as in Fig.6

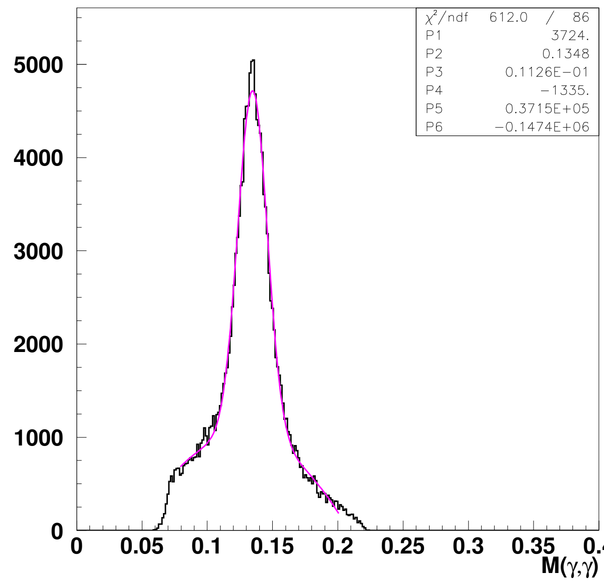

FIG. 10. Reconstructed π^0 mass from energy deposited in BigCal. An energy resolution of 8.2% has been observed.

of the mass peak in a histogram of the mass distribution of the events was fitted and the centroid value divided by the neutral pion mass. This ratio was taken as the new gain parameter. The procedure was iterated until the parameters converged. The neural network was crucial in obtaining the correct angle and energy corrections. Figure 10 illustrates the pion mass resolution obtained by this procedure. This resolution is directly proportional to the cluster energy resolution of BigCal.

During the early part of the experiment BigCal opened the trigger. As a result, the Čerenkov's timing depended on which of BigCal's rows had triggered the event. The top panel of Figure 11 shows the uncorrected Čerenkov time distribution versus BigCal's triggering rows, for one of the Čerenkov mirrors. The region of the peaks corresponds to those rows included in the geometric projection of this mirror onto BigCal. To decrease the background after the cut cerenkov TDC the time distribution for each row was fitted with a Gaussian and the peak shifted to zero. This procedure decreased the width of the one dimensional time distribution and therefore decreases the background. The bottom panel of Figure 11 shows the timing distribution after the alignment.

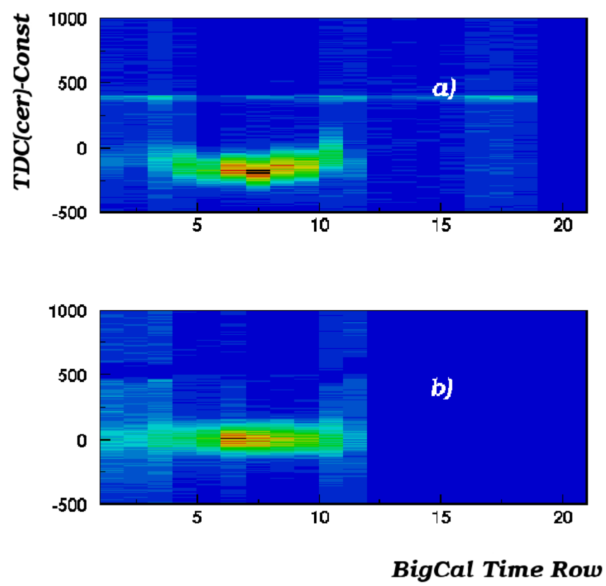

FIG. 11. Čerenkov timing peak versus BigCal triggering row. Top panel, a), uncorrected; bottom panel, b), corrected.

A. Cerenkov Electron Identification

B. Tracking

C. Binning

V. EXTRACTION OF ASYMMETRY

A. Charge Normalization

B. Live time correction

For reasons that we have been unable to establish, only information about the total number of triggers and the number of triggers of one of the helicity signs were recorded. In addition to the resulting ambiguity about the helicity of the recorded triggers, this issue made it impossible to calculate the livetime in the conventional way.

$$l = \frac{N_{triggers}}{N_{scalers}} \tag{12}$$

As a solution we used the scaler and trigger information for negative helicity only. For each run we plotted the livetime corresponding to negative helicity versus the number of electrons, based on the number of recorded events. The distribution was parametrized using a second degree polynomial. Figure 12 shows the distribution of livetime versus number of recorded triggers for negative helicity events for one of the runs. The fitted histogram is the profile of the distribution. The fit was used to calculate the livetime for both helicity signs, using only the the number of recorded electrons. To decrease the uncertainty due to the fit, the region of the fit was set as good region. Data outside that region were not used in the analysis. The procedure was done for each analyzed run to take into account any changes from run to run (like efficiency of the detectors, thresholds, or dead channels).

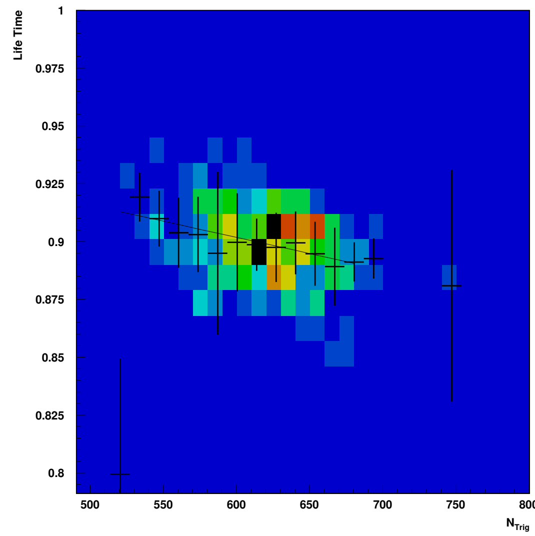

FIG. 12. Livetime dependence on the number of recorded triggers for negative helicity events. The fitted histogram is the profile of the distribution.

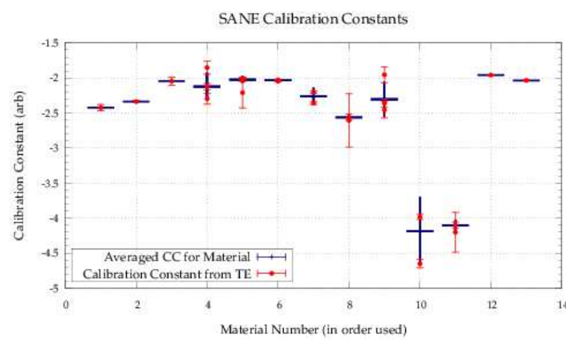

FIG. 13. Calibration constants for each SANE target material.

C. Beam Polarization

D. Target Polarization

Final target polarization data were produced for each experimental run from NMR signals taken in time, and required calibration and other correction. A calibration constant was calculated for each point in a thermal equilibrium measurement, and these constants were averaged together to produce a constant for each measurement. After calibrations for each measurement were produced, a single average calibration constant was created for each material. Figure 13 shows calibration constants for all SANE materials. Materials 10 and 11 in the figure have vastly different calibrations due to a different orientation of the NMR coil during their use.

NMR signals for each event were baseline subtracted, integrated, and scaled by the appropriate calibration constant for the material to produce polarization data in time. These data were then corrected for gain factor discrepancies in the NMR circuitry. A slight drift in the target's magnetic field also necessitated a correction in the fitting process which removes the baseline from the NMR signal. Once a polarization was calculated for each event, these events were averaged, weighted by charge deposited during the event, into one polarization for each experiment run. Figure 14 shows the charge averaged target polarizations throughout the experiment. The average polarization over the entire experiment was 68%.

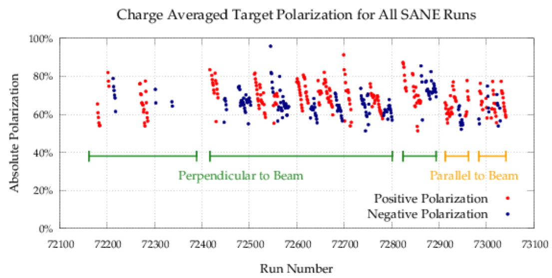

FIG. 14. Charge averaged target polarization for each SANE experimental run, showing run ranges for perpendicular and parallel magnetic field configurations.

E. Packing Fraction

F. Target Dilution Factor

The dilution factors df are needed to correct the raw asymmetries for the contributions of the unpolarized nucleons in the target. It is the kinematics dependent ratio of cross-sections from the protons to cross-sections from all the materials in the NH_3 target sample. A dilution factor is necessary for each and every target load used during running of SANE.

In order to get dilution factors one must first get packing fractions. A packing fraction is essentially the amount of target material in the target cup. Similar to dilution factors, a packing fraction is needed for each target load used during the experiment. However a packing fraction is a percentage and independent of kinematics. The packing fractions are obtained from HMS (High Momentum Spectrometer) data where a carbon target was used. The carbon target is used because its cross-sections are well known and it is very similar to nitrogen, which is a significant part of the NH_3 target sample. A detailed description of how the packing fractions were obtained is given in the section on packing fractions.

The dilution factors originate from measuring the counts $N^{+,-}$ for each helicity from all materials in the target region, seen by the detectors, forming a raw asymmetry

$$A_{raw} = \frac{N^+ - N^-}{N^+ + N^-} = \frac{N^+ - N^-}{sum_{all}}$$

Unpolarized counts cancel in the numerator, but not in the denominator, so the numerator is actually $N^+_{proton} - N^-_{proton}$. We want the asymmetry for the proton only

$$A_{proton} = \frac{N^+_{proton} - N^-_{proton}}{sum_{proton}}$$

This can then be written as

$$A_{raw} = \frac{N^+_{proton} - N^-_{proton}}{sum_{proton}} * \frac{sum_{proton}}{sum_{all}} = A_{proton} * df$$

The role the dilution factors play is that they are the ratio of rates of free polarizable nucleons (proton) to all nucleons composing the total target (helium, nitrogen, ...). This is kinematics dependant. For each target load, used during the running of the experiment, a dilution factor is needed. The amount of time needed to obtain a statistical error ΔA has a time dependence $t \propto \frac{1}{df}$.

The dilution factor, dependent on the 4-momentum transfer Q^2 and invariant mass of final states W, is defined

$$df(Q^2, W) = \frac{C_1\, \sigma_1(Q^2, W)}{\sum_A C_A\, \sigma_A(Q^2, W)}$$

Here, A is the atomic number for all the nucleons making up the target sample and C_A a constant that accounts for the packing-fraction dependent density, effective length, and A. This calculation was previously used for the RSS analysis [11].

The dilution factors were obtained in several steps. MC events are generated, on the order of 10^6, using the cross-section model F1F209 [12, 13]. The MC is GEANT based [14], applying both external and internal radiative corrections [15]. The kinematic quantities are calculated using energy and position reconstructed via artificial neural network. The standard set of cuts are applied to the MC, which are also used for data. The $df(Q^2, W), df(Q^2, x)$ ratios are then calculated using the packing fractions that were obtained with the HMS information. These ratios are binned similar to the data, based on the reconstructed energy resolution [16].

The obtained df ratios have an average value of 0.18, which is close to the expected value (Fig. 15). As a check, some df were calculated with the F1F209. There is very good agreement between these. The radiative corrections don't seem to be significant in the kinematic regions of interest. This was checked by comparing the radiative corrected cross-sections with the uncorrected Born cross-sections. The expected contribution to systematics is approximately 5%.

G. Measured Asymmetries

VI. RADIATIVE AND BACKGROUND CORRECTIONS

A. Radiative Elastic tail subtraction

B. Pair-symmetric background subtraction

One of the contributions to the physics asymmetry can come from the pair symmetric background, that cannot

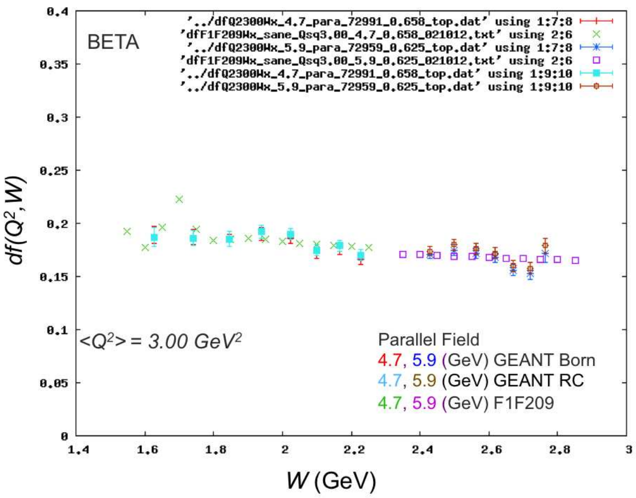

FIG. 15. Dilution factor for one of the NH_3 target loads as a function of W(GeV). This is for a parallel target magnet field configuration, for both energies. The apparent structures for $W < 2$ represent some of the resonances for the proton.

be distinguished from the signal of inelastic electrons because of the non-magnetic nature of BETA.

Neutral pions are produced inside the target by direct electroproduction and by beam bremsstrahlung. These pions decay through Dalitz processes and produce electron-positron (e^-,e^+) pairs directly, or decay into two photons which then convert into pairs. Since the Cerenkov cannot distinguish between the directly scattered electrons and those associated with pairs, the detected asymmetry A_{calc} is diluted by the number of electrons or positrons from pairs, and affected by the pairs asymmetry (if any).

To obtain the physics asymmetry A_{phys} from A_{calc} we define

$$A_{calc} = \frac{N^+ - N^- + N_p^+ - N_p^-}{N^+ + N^- + N_p^+ + N_p^-} = A_{phys} \cdot d_f^p + A_{pair} \cdot (1 - d_f^p) \quad (13)$$

where

$$d_f^p = \frac{N^+ + N^-}{N^+ + N^- + N_p^+ + N_p^-} \quad (14)$$

is a dilution factor due to the pair-symmetric background and

$$A_{phys} = \frac{N^+ - N^-}{N^+ + N^-} \quad (15)$$

$$A_{pair} = \frac{N_p^+ - N_p^-}{N_p^+ + N_p^-} \quad (16)$$

are the physics and pairs asymmetry, respectively.

Any asymmetry of the pairs would originate from an asymmetry of the π^0. As the first step to correct for the pair symmetric contribution, we calculated the neutral pion asymmetry using our data. For this purpose we used two photon events to reconstruct neutral pions. The final asymmetry obtained from the data is consistent with zero, as discussed in detail in sec. VI C

As it was mentioned above we had two major sources of pair symmetric background. The first source is from pairs that originate at the target from π^0 decay. Due to the polarized target magnetic field we only detect either the electron or the positron. The other particle is swept away from the detectors. The second source comes from the conversion of photons in the materials outside the region of intense target magnetic field, where the deflections by the field are too small to separate the members of the pair, which is detected as single cluster with larger energy than in the first case.

To estimate the contribution of the pair symmetric background we used the `epc` code [17] to generate photo- and electroproduced π^0's at the target. Then, using GEANT, we propagated the decay particles through the detector setup. The simulated energy and coordinate distributions of the pair-symmetric background are not uniform due to the strong target magnetic field. To control this effect we divided BIGCAL into 100 equally sized segments and calculated the background dilution for each segment. The final correction is a function of the coordinates at BIGCAL and of the cluster energy. Figure 16 shows fair agreement between the full Monte Carlo, which includes pair-symmetric background and direct electrons, and the data, for different coordinate bins on BigCal.

At the same time we checked if the number of simulated neutral pions is close to the experimental observation. To select pion events in the simulation we selected two-cluster events with combined energies greater than 1 GeV (to have almost the same condition on cluster energy cut as in the data analysis, and to avoid issues with detector thresholds), no Cerenkov hit for both clusters, and the trigger condition that clusters should be located in different quarters of BigCal. In addition we removed the edges of BigCal by applying cuts on the cluster coordinates, $|X_{clust}| < 52$ cm and $|Y_{clust}| < 100$ cm, for both clusters. We also applied a cut on the number of cells in the cluster to be $N_{cell} > 4$.

Figure 17 shows on panel a) the energy spectrum of generated neutral pions from reconstruction of two neutral cluster events; panel b) shows the simulated energy spectrum of the reconstructed charged particles with a hit in the Cerenkov; panel c) is the reconstructed mass of neutral pions in the data; and panel d) shows the energy spectrum of the reconstructed charged particles in the data.

The ratio of MC pions to MC charged particles is 0.0038, while the same ratio for the data is 0.0016. The difference can come from trigger efficiency, detector efficiency and detector channels with higher thresholds than others. The data show almost a factor of two fewer pions than predicted from the MC. This discrepancy can come from extra charged particle background which creates a

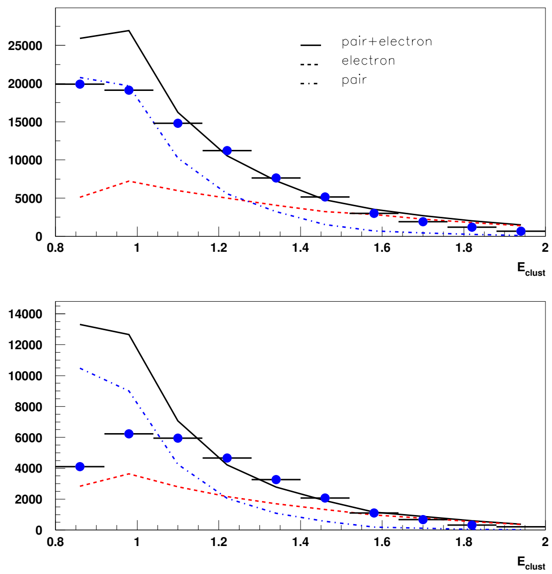

FIG. 16. Energy distribution for two different parts of BigCal. Filled circles show the data, the solid line shows the combined simulation of electron scattering and pair-symmetric background, the dashed line shows the simulation of electron scattering only, and the dashed-dotted line shows the simulation of the pair-symmetric background only.

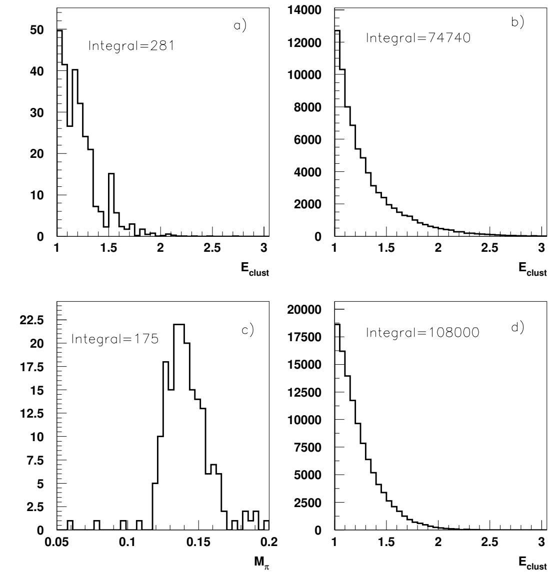

FIG. 17. Figure a) Simulated energy spectrum of generated neutral pions from reconstruction of two neutral cluster events; b) Simulated energy spectrum of the reconstructed charged particles with a hit in the Cerenkov; c) Reconstructed neutral pions from data; d) Energy spectrum of the reconstructed charged particles with a hit in the Cerenkov from data.

hit in Cerenkov, or from events with a third cluster in BigCal.

C. Pion asymmetry

Pair symmetric processes create a background to inclusive electron scattering. In SANE, Positron–electron pair constitutes the main source of background which comes from π^0 decay. A π^0 is created as the electron beam traverses the target and quickly decays into two photons which convert to positron–electron pair in the target. In creating electron–positron pairs, these processes provide additional electrons that can enter our detector setup (BETA) and are indistinguishable from an outgoing DIS electron.

To extract the physics asymmetries and meet the experimental goals, the background contributions to the measured asymmetry must be well understood.

Lepton pair production from bremsstrahlung photons is negligible for SANE. Also, $\pi^{+,-}$ and kaons do not affect because they are removed by BigCal as they deposit less energy than electrons and are less ionizing.

The dominant decay of the π^0 is to two photons $\pi^0 \rightarrow \gamma\gamma$ with a branching ratio of 98.8%. The remaining 1.2% follows the Dalitz decay mode, $\pi^0 \rightarrow \gamma e^+ e^-$

The π^0 asymmetry is calculated by the reconstruction of π^0 mass from energy deposited in BigCal from events with two clusters produced by neutral particles. The identification of π^0 is done by placing a cut on π^0 mass and using E > 0.6 GeV energy cut; at high energy π^0 have low contribution, whereas below 0.5 GeV the neural network does not work. The raw pion asymmetry A_{Raw} is defined as

$$A_{raw} = \frac{N^+/C^+ - N^-/C^-}{N^+/C^+ + N^-/C^-} \tag{17}$$

where $N^{+(-)}$ is the number of counts with i_helicity positive (negative), $C^{+(-)}$ is the incoming charge accumulated during that event with positive (negative) helicity.

The Physics Asymmetry is gotten by considering the target and beam polarizations, P_t and P_b respectively

$$A_{physics} = \frac{1}{P_t P_b} A_{raw} \tag{18}$$

Figure 18 below shows the total average asymmetries of the neutral pions – the red indicates the average raw asymmetry while the blue indicates the average physics asymmetry. The green indicates the product of the beam and target polarizations ($P_b P_t$), which were on average

73% and 70% for the beam and target polarization, respectively. In Fig. 18 the product $P_b P_t$ has been scaled by a factor so as to fit in the same plot.

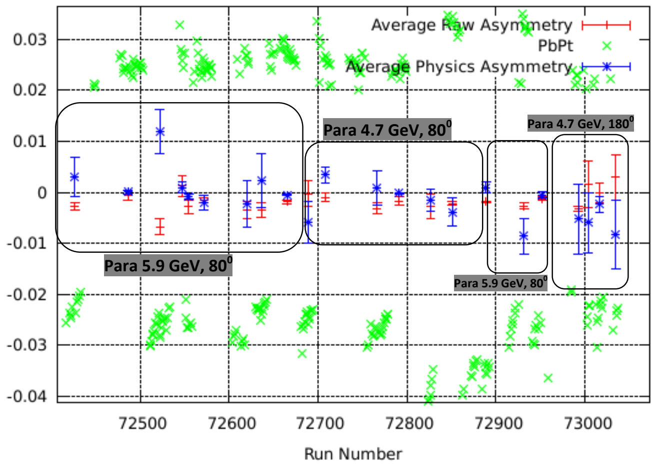

FIG. 18. Average Raw (crosses) and Physics Asymmetries (stars), plotted along the product of beam and target polarization, P_t, P_b (diagonal crosses).

TABLE I. Pion asymmetries

Energy & orientation	Physics Asymmetry
5.9 GeV, 80°	0.0004 +/- 0.0020
4.7 GeV, 80°	0.0047 +/- 0.0047
5.9 GeV, 180°	-0.0116 +/- 0.0074
4.7 GeV, 180°	0.0071 +/- 0.0103
$\langle A_{Physics} \rangle$	-0.0008 +/- 0.0018

From this we can conclude that the total asymmetry of the neutral pion is consistent with zero and the π^0 contribution is more of a background dilution rather than an asymmetry. Even though the neutral pion data show that the asymmetry is zero with errors, the errors of this result will propagate to the systematic uncertainties of the background corrected asymmetries of about 10% `(need firmer number)`.

D. Inelastic radiative corrections

Internal radiative corrections in inclusive and semi-inclusive DIS off polarized protons were performed using POLRAD 2.0 [18]. Due to lack of good experimental data in the region of interest as an input to POLRAD we used several models which are based on either current knowledge of parton distribution functions (Leader 2006, AAC) or global fit to existing data (CLAS Model) and several toy models which are based on some observations from our data. Toy models were based on distributions of $1/\nu g_1/F_1$ and $1/\nu^2 g_2/F_1$. Experimental data showed very small dependence of $1/\nu g_1/F_1$ and $1/\nu^2 g_2/F_1$ versus $1/\nu$ distributions for different Q^2. Figure 19 shows $1/\nu g_1/F_1$ and $1/\nu^2 g_2/F_1$ obtained from data after multiple iterations with POLRAD 2.0 using toy model 0 for g_1 and and g_2. Curves represent different fits using

- g_1 Model 0 - $\frac{1}{\nu}\frac{g_1}{F_1} = \frac{1}{\nu} \cdot p_1$
- g_1 Model 1 - $\frac{1}{\nu}\frac{g_1}{F_1} = \frac{1}{\nu} * \frac{(p_1 * \frac{1}{\nu^4} + p_2)}{(p_1 * \frac{1}{\nu^4} + p_3)}$
- g_1 Model 2 - $\frac{1}{\nu}\frac{g_1}{F_1} = \frac{0.6}{\nu} * \frac{(p_1 * \frac{1}{\nu^4} + p_2)}{(p_1 * \frac{1}{\nu^4} + p_3)}$
- g_2 Model 0 - $\frac{1}{\nu}\frac{g_2}{F_1} = \frac{1}{\nu^2} \cdot p_1$
- g_2 Model 1 - $\frac{1}{\nu}\frac{g_2}{F_1} = \frac{1}{\nu^2} \cdot p_1 + \frac{1}{\nu} \cdot p_2$

which were used in different combinations to estimate systematic errors from internal radiative correction. Several iterations were performed using this models to achieve stability of the correction for A_1 and A_2. As a starting point we obtain g_1 and g_2 from fit to uncorrected data. Using the results we calculate the corrections to A_1 and A_2. Then we refit g_1 and g_2 and repeat the procedure. Figure 20 shows that A_1 and A_2 corrections converge after about 3 iterations. Figure 21 shows internal radiative corrections to A_1 and A_2 versus Bjorken x for different models including AAC, Leader and CLAS. It is important to note that the correction to data and the uncertainty increases at low x. As final corrections we will use results obtained from CLAS fit.

VII. SPIN ASYMMETRIES

A. Systematic errors

The systematic errors of the data come from several sources, listed in Table II for the normalizations and Table III for the kinematics dependent uncertainties.

First, a relatively small source of the systematics comes from the bin size. To calculate the kinematic coefficients to obtain the spin asymmetries A_1 and A_2 from the measured asymmetries $A_\parallel$ and A_{80} we use an average value of the scattered electron energy E' and angle θ_e. This creates a systematic uncertainty which can be estimated by calculating the asymmetry at the edges of the bins and taking the standard deviation from the mean value.

The next source of systematic errors is associated with the target polarization. To estimate the effect we gathered several thermal equilibrium measurements. The average error associated with target polarization uncertainty is estimated to be about 5%.

`needs better discussion of the` P_{target} `systematics. James?`

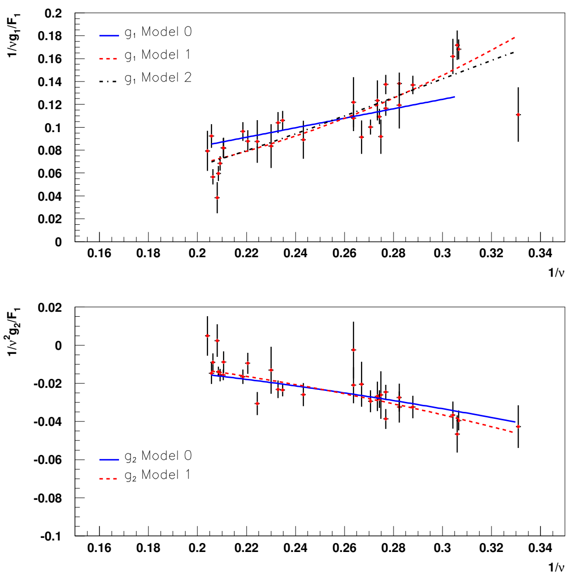

FIG. 19. $1/\nu g_1/F_1$ and $1/\nu^2 g_2/F_1$ obtained from data after multiple iterations with POLRAD 2.0 using toy model 0 for g_1 and and g_2. Curves represent different toy model fits.

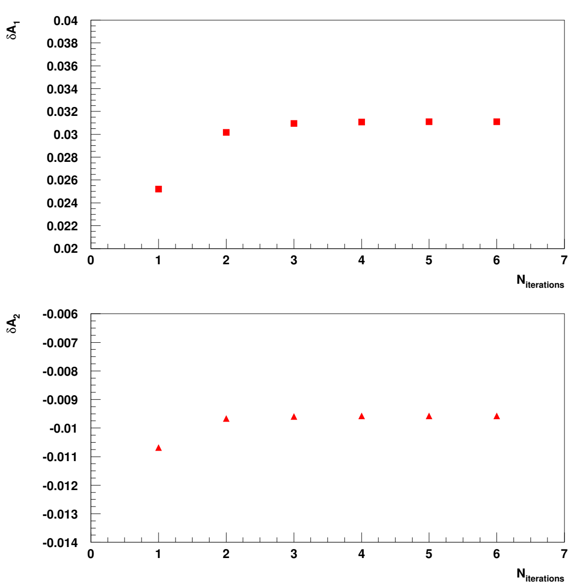

FIG. 20. A_1 and A_2 internal radiative correction versus number of iterations for one data poin using g_1 model 2 and g_2 model 0.

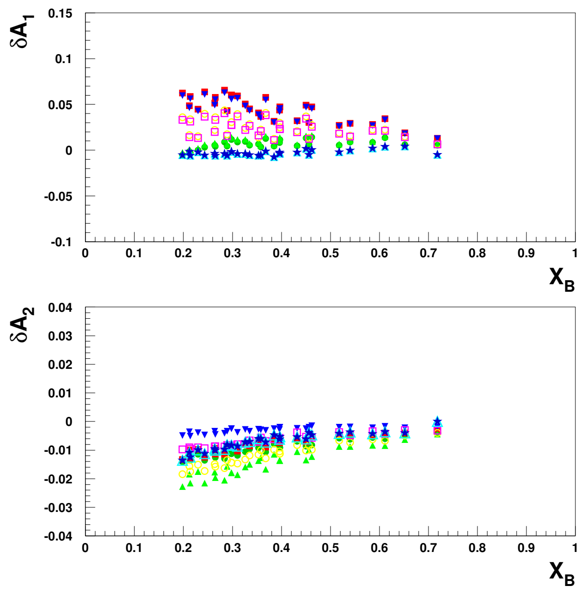

FIG. 21. A_1 and A_2 internal radiative correction versus Bjorken x.

TABLE II. Normalization errors

Source	Relative error on asymmetry
P_{target}	5%
P_{beam}	x %

The biggest contributions to the systematic errors comes from the internal radiative corrections and from the e^+ - e^- pairs backgground.

Figure 17 shows that at small energies the pion contribution rises faster than the electron contribution. To estimate the systematic uncertainty associated with pion contamination we varied the amount of the NH_3 material in Monte Carlo simulation by about 5% which is equal to the uncertainty in packing fraction and amount of the material in which pair conversion can occure by 10% and then calculated effect of this change to the dilution factor

TABLE III. Kinematics-dependent errors

Source	Relative error	Error on asymmetry
Dilution factor	5%	2% (relative)
Pair background	15%	3% (relative)
Radiative tail	2%(?)	1%(?)
Inelastic radiative corrections	3% (?)	
etc	etc	etc

associated with pair symmetric background.

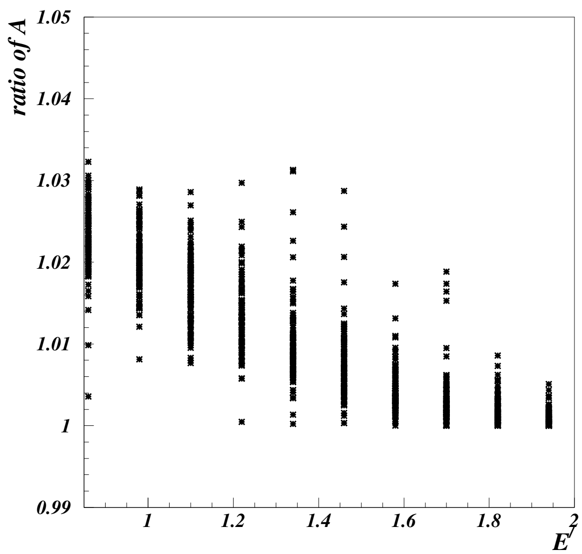

FIG. 22. Ratio between the asymmetry calculated with 5% increase of the NH_3 in target and 10% increase of the material in which pair conversion can occure to the base asymmetry.

Figure 22 shows ratio between the asymmetry calculated with 5% increase of the NH_3 in target and 10% increase of the material in which pair conversion can occure to the initial asymmetry. The systematic uncertainty from this effect is rather small but it is energy dependent. The main uncertainty associated with pair-symmetric background comes from the model estimation of the number of produced pairs. From the data we obtained that the number of pions we reconstruct are smaller by the factor of two from what we should obtain from Monte-Carlo. This can come either from inefficiency of the two cluster trigger or due to the fact that the model we are using is incomplete. Taking into acoount this effect we estimated the relative error and parametrized as function of energy $\delta\sigma = 0.15/e^{E'} \cdot A$.

The systematic uncertainty associated with internal radiative corrections we obtained using the results for the asymmetry obtained from different models and taking the standard deviation from the mean Figure 20.

The uncertainty in packing fraction contributes to the systematic uncertainty not only through the pair-symmetric background but also through the dilution factor directly. Although due to the difference in cross-section between hydrogen and heavier nuclei the 5% effect in packing fraction transfers to about 2% in Asymmetry. It is important to note that with increase of the packing fraction the dilution factor from pair-symmetric baground is smaller but at the same time the dilution factor from simple nuclon counting is larger. So these two effects are partially canceling each other.

VIII. SPIN STRUCTURE FUNCTIONS

IX. CONCLUSION

[1] SLAC E80, M. J. Alguard *et al.*, Phys. Rev. Lett. **37**, 1261 (1976); **41**, 70 (1978).
[2] SLAC E130, G. Baum *et al.*, Phys. Rev. Lett. **51**, 1135 (1983).
[3] EMC, J. Ashman *et al.*, Nucl. Phys. **B328**, 1 (1989)
[4] SLAC E142, P. L. Anthony *et al.*, Phys. Rev. Lett. **71**, 959 (1993).
[5] SLAC E154, K. Abe *et al.*, Phys. Rev Lett. 79 (1997) 26.
[6] A. Airapetian *et al.*[HERMES Collaboration], hep-ex/0609039
[7] SLAC E143, K. Abe *et al.*, Phys. Rev. D **58**, 112003 (1998).
[8] SMC, B. Adeva *et al.*, Phys. Rev. D **58** 112001-1 (1998).
[9] SLAC E155, K. Abe *et al.*, Phys. Lett. **B463**, 339 (1999).
[10] P. L. Anthony *et al.*[E155 Collaboration], Phys. Lett. **B458**, 529 (1999).
[11] P. L. Anthony *et al.*[E155 Collaboration], Phys. Lett. **B553**, 18 (2003).
[12] A. Airapetian *et al.* [HERMES Collaboration], Phys. Rev. Lett. **92**, 012005 (2004)
[13] B. Adeva *et al.* [Spin Muon Collaboration], Phys. Lett. B **420**, 180 (1998)
[14] E. S. Ageev *et al.* [COMPASS Collaboration], Phys. Lett. B **633**, 25 (2006)
[15] A. Airapetian *et al.* [HERMES Collaboration], Phys. Rev. Lett. **84**, 2584 (2000)
[16] K. V. Dharmawardane *et al.* [CLAS Collaboration], Phys. Lett. B **641**, 11 (2006)
[17] X. Zheng *et al.* [Jefferson Lab Hall A Collaboration], Phys. Rev. Lett. **92**, 012004 (2004)
[18] P. J. Mulders and R. D. Tangerman, Nucl. Phys. B **461**, 197 (1996) [Erratum-ibid. B **484**, 538 (1997)] [hep-ph/9510301].
[19] A. M. Kotzinian and P. J. Mulders, Phys. Rev. D **54**, 1229 (1996) [hep-ph/9511420].
[20] R. D. Tangerman and P. J. Mulders, hep-ph/9408305.
[21] R. L. Jaffe, Comments Nucl. Part. Phys. **19**, 239 (1990); arXiv:hep-ph/9602236.
[22] S. Wandzura and F. Wilczek, Phys. Lett. B172 (1977) 195.
[23] J. L. Cortes, B. Pire and J. P. Ralston, Z. Phys. C55 (1992) 409.
[24] R. L. Jaffe and Xiangdong Ji, Phys. Rev. **D 67** (1991) 552.

[25] X. Artru and M. Mekfi, Z. Phys. C **45**, 669 (1990).
[26] M. Göckeler *et al.*, Phys. Rev. D **72** 054507 (2005).
[27] K. Slifer *et al.* [Resonance Spin Structure Collaboration], Phys. Rev. Lett. **105**, 101601 (2010)
[28] E. Stein *et al.*, Phys. Lett. B **343**, 369 (1995).
[29] I. Balitsky *et al.*, Phys. Lett. B **242**, 245 (1990); B **318**, 648 (1993) (Erratum).
[30] B. Ehrensperger and A. Schäffer, Phys. Rev. D **52**, 2709 (1995).
[31] M. Stratmann, Z. Phys. C **60**, 763 (1993), and private communication for values at $Q^2 = 5$ (GeV/c)^2.
[32] H. Weigel, L. Gamberg and H. Reinhart, Phys. Rev. D **55**, 6910 (1997).
[33] M. Wakamatsu, Phys. Lett. B **487**, 118 (2000), and private communication.
[34] X. Ji, hep-ph/9510362.
[35] E. Stein, P. Gornicki, L. Mankiewicz and A. Schafer, Phys. Lett. B **353**, 107 (1995); E. V. Shuryak and A. I. Vainshtein, Nucl. Phys. B **201**, 141 (1982); Philippe Grenier, *Etude des Fonctions de Structure en Spin du Nucleon: L'Experience E143 au SLAC*, Ph. D. Thesis, Saclay 1995, unpublished.
[1] D. G. Crabb and W. Meyer, Annual Review of Nuclear and Particle Science **47**, 67 (1997).
[2] K. A. et al. ((E143 Collaboration)), Phys. Rev. D **58**, 112003 (1998).
[3] P. L. e. a. Anthony (E155), Phys. Lett. **B458**, 529 (1999), arXiv:hep-ex/9901006.
[4] P. L. e. a. Anthony (E155), Phys. Lett. **B553**, 18 (2003), arXiv:hep-ex/0204028.
[5] H. e. a. Zhu, Phys. Rev. Lett. **87**, 081801 (2001).
[6] M. Borghini, CERN-68-32.
[7] A. Abragam, *The Principles of Nuclear Magnetism* (Clarendon Press, Oxford, 1961).
[8] G. Court, D. Gifford, P. Harrison, W. Heyes, and M. Houlden, Nuclear Instruments and Methods in Physics Research Section A: Accelerators, Spectrometers, Detectors and Associated Equipment **324**, 433 (1993).
[9] T. J. Liu, T. D. Averett, D. G. Crabb, D. B. Day, J. S. McCarthy, and O. A. Rondon, Nuclear Instruments and Methods in Physics Research Section A: Accelerators, Spectrometers, Detectors and Associated Equipment **405**, 1 (1998).
[10] P. M. McKee, Nuclear Instruments and Methods in Physics Research Section A: Accelerators, Spectrometers, Detectors and Associated Equipment **526**, 60 (2004), proceedings of the Ninth International Workshop on Polarized Solid Targets and Techniques.
[11] O. A. Rondon, RSS T. N. 2005-03 (2006).
[12] P. E. B. M. E. Christy, **81**, 055213 (2010).
[13] M. E. C. P. E. Bosted, Phys.Rev. C **77**, 065206 (2008).
[14] G. Warren, (2003).
[15] Y. S. T. L. W. Mo, Rev. Mod. Phys. **41**, 205 (1969).
[16] J. Mulholland, (2011).
[17] J. W. Lightbody and J. S. O'Connell, Computers in Physics **2** (1988).
[18] I. Akushevich, A. Ilyichev, N. Shumeiko, A. Soroko, and A. Tolkachev, Comput.Phys.Commun. **104**, 201 (1997), arXiv:hep-ph/9706516 [hep-ph]

[1] D. G. Crabb and W. Meyer, Annual Review of Nuclear and Particle Science **47**, 67 (1997).
[2] K. A. et al. ((E143 Collaboration)), Phys. Rev. D **58**, 112003 (1998).
[3] P. L. e. a. Anthony (E155), Phys. Lett. **B458**, 529 (1999), arXiv:hep-ex/9901006.
[4] P. L. e. a. Anthony (E155), Phys. Lett. **B553**, 18 (2003), arXiv:hep-ex/0204028.
[5] H. e. a. Zhu, Phys. Rev. Lett. **87**, 081801 (2001).
[6] M. Borghini, CERN-68-32.
[7] A. Abragam, *The Principles of Nuclear Magnetism* (Clarendon Press, Oxford, 1961).
[8] G. Court, D. Gifford, P. Harrison, W. Heyes, and M. Houlden, Nuclear Instruments and Methods in Physics Research Section A: Accelerators, Spectrometers, Detectors and Associated Equipment **324**, 433 (1993).
[9] T. J. Liu, T. D. Averett, D. G. Crabb, D. B. Day, J. S. McCarthy, and O. A. Rondon, Nuclear Instruments and Methods in Physics Research Section A: Accelerators, Spectrometers, Detectors and Associated Equipment **405**, 1 (1998).
[10] P. M. McKee, Nuclear Instruments and Methods in Physics Research Section A: Accelerators, Spectrometers, Detectors and Associated Equipment **526**, 60 (2004), proceedings of the Ninth International Workshop on Polarized Solid Targets and Techniques.
[11] O. A. Rondon, RSS T. N. 2005-03 (2006).
[12] P. E. B. M. E. Christy, **81**, 055213 (2010).
[13] M. E. C. P. E. Bosted, Phys.Rev. C **77**, 065206 (2008).
[14] G. Warren, (2003).
[15] Y. S. T. L. W. Mo, Rev. Mod. Phys. **41**, 205 (1969).
[16] J. Mulholland, (2011).
[17] J. W. Lightbody and J. S. O'Connell, Computers in Physics **2** (1988).
[18] I. Akushevich, A. Ilyichev, N. Shumeiko, A. Soroko, and A. Tolkachev, Comput.Phys.Commun. **104**, 201 (1997), arXiv:hep-ph/9706516 [hep-ph].